Three-photon population imaging of subcortical brain regions - Supplementary information

Contents

Supplementary Note 1: Optimizing sampling rates for 3P calcium imaging of neuronal activity with GCaMP6s . . . 3
1.1 Optimizing the spatial sampling rate . . . 3
Supplementary Fig. 1: The fidelity of cell segmentation for sparse spatial sampling . . . 4
1.2 Optimizing the temporal sampling rate . . . 5
Supplementary Fig. 2: The fidelity of calcium event extraction as a function of frame rate . . . 5
1.3 A general framework for sampling optimization . . . 5
Supplementary Fig. 3: The effect of focal spot spacing on the imaging of astrocytic processes 7

Supplementary Note 2: Imaging improvement due to sampling optimization . . . 8
Supplementary Fig. 4: A comparison of the sampling schemes used in conventional microscopy and LIFT . . . 9
Supplementary Fig. 5: Heating simulation results . . . 10

Supplementary Note 3: The challenges in using conventional beam scanning mechanisms in large FOV 3P imaging . . . 13

Supplementary Fig. 6: Detailed system schematic . . . 15

Supplementary Fig. 7: A comparison of denoising and filtering for postprocessing of datasets . . . 16

Supplementary Fig. 8: A comparison of traces from denoised data and filtered data . . . 17

Supplementary Fig. 9: The point spread function of LIFT scope and the uniformity over its field of view 18

Supplementary Fig. 10: Statistical analysis of run versus rest neuronal activity . . . 19

Supplementary Fig. 11: 3P population imaging in the mouse hippocampus at video rate . . . 20

Supplementary Fig. 12: High-resolution 3P calcium imaging in the mouse hippocampus . . . 21

Supplementary Fig. 13: Scan waveform and focal spot spacing . . . 22

Supplementary Fig. 14: Field of view geometry . . . 23

Supplementary Fig. 15: A rescan of a neuronal population in the mouse hippocampus . . . 24

Supplementary Fig. 16: Structural and functional imaging of brain areas dorsal to the rescanned neuronal population . . . 25

Supplementary Table 1: Comparison of LIFT to other 3P systems capable of performing calcium imaging at 1 mm depth . . . 26

Supplementary Table 2: Component list for LIFT . . . 27

Supplementary Table 3: Acquisition parameters for all figures . . . 28

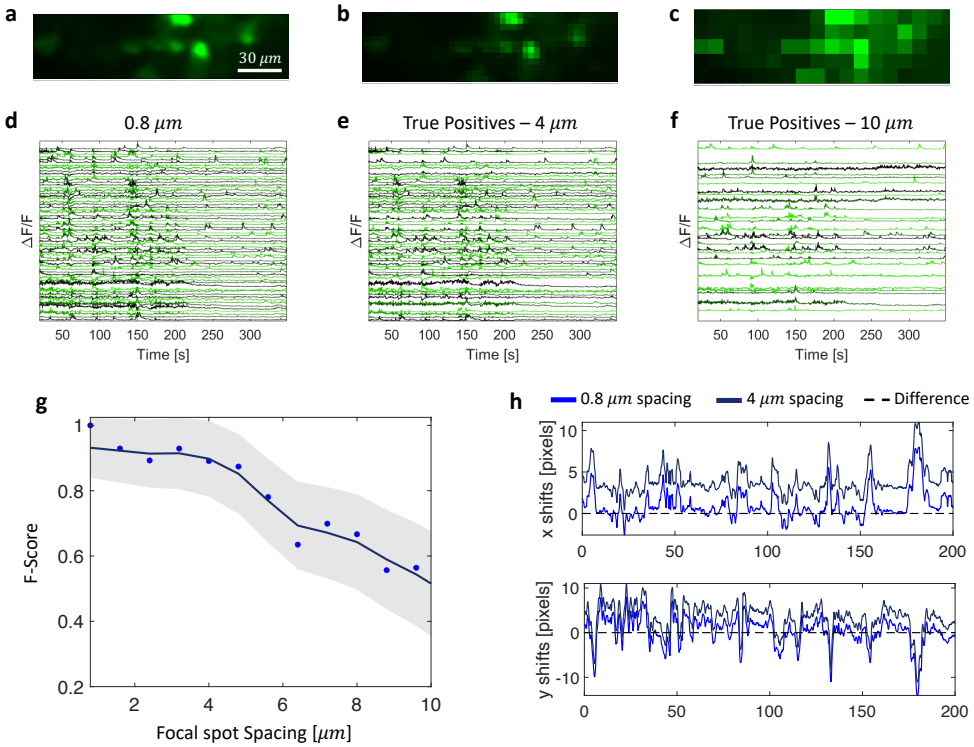
Supplementary Note 1: Optimizing sampling rates for 3P calcium imaging of neuronal activity with GCaMP6s

1.1 Optimizing the spatial sampling rate

The desirable focal spot spacing for 3P calcium imaging of neuronal activity is the largest spacing that allows to spatially resolve cells and does not significantly affect the fidelity of cell segmentation. In order to find that spacing, we performed a systematic study of how focal spot spacing affects fidelity. First, we recorded a time series of calcium activity in a mouse hippocampus labeled with GCaMP6s, with small focal spot spacing (0.8 μm). The dataset was denoised, motion-corrected and filtered to remove galvo-related artifacts, following our usual data analysis pipeline (see Methods). Then data points were removed to create additional time series with a gradually increasing focal spot spacing, from 1.6 μm to 10.4 μm (Supplementary Fig. 1a-c). Those time series were then analyzed by our software that is based on CNMF. Due to the downsampling, cells appear to be different sizes in the different time series, necessitating a different parameter set as an input for CNMF for each one. To avoid extensive parameter sweeps within CNMF's large parameter space, which introduce variability and can skew results, we upsampled the resulting time series back to the native resolution using bicubic interpolation in Matlab before analyzing them with our software.

The result was a set of ROIs for each time series and the corresponding activity traces (Supplementary Fig. 1d-f). To assess the fidelity of the ROI set retrieved for a particular large focal spot spacing, the correlation coefficient between each ROI retrieved from the large spacing set and all ROIs retrieved from the 0.8 μm spacing set was computed. For each ROI in the 0.8 μm dataset, the ROI from the large spacing set that had the highest correlation with it was chosen. A threshold of 0.6 correlation between the chosen ROI and the 0.8 μm dataset ROI was selected to determine whether the neuron was detected. This procedure was repeated for all ROIs in the 0.8 μm dataset. The true positive rate was computed as the number of detected cells in the large spacing set divided by the number of detected cells in the 0.8 μm data. False positive and false negative rates were computed in a similar manner, compared to the 0.8 μm data. Finally, the F-score [1] was computed from $\frac{TP}{TP+\frac{1}{2}(FN+FP)}$, where TP, FN, and FP are the true positive rate, false negative rate and false positive rate, respectively. The variance in F-score was computed by splitting the FOV of the original dataset into five and running this analysis pipeline on each of those datasets, in order to exclude variance associated with signal-to-noise ratio (SNR), cell density, expression levels, etc.

The resulting plot shows a decreasing F-score with increasing focal spot spacing (Fig. 1g and S1), with the shaded region indicating the computed variance. However, the reduction in F-score from 0.8 μm to 4-5 μm focal spot spacing is minor, with the F-score only dropping by approximately 3% - less than the variance in cell segmentation resulting from the analysis with CNMF. The F-score starts to decline rapidly from 5-6 μm spacing and above, making 4 μm spacing optimal. Since the F-score of the 0.8 μm dataset is calculated against itself, the fit excludes that data point.



Supplementary Fig. 1 The fidelity of cell segmentation for sparse spatial sampling. (a)-(c) An example, zoomed-in section of the maximum intensity projection of the datasets with 0.8 μm, 4 μm, and 10 μm sampling, respectively. (d) The extracted traces for the 0.8 μm dataset. (e) The extracted traces from the 4 μm dataset, for the ROIs considered true positives when compared to the 0.8 μm dataset. (f) The extracted traces from the 10 μm dataset, for the ROIs considered true positives when compared to the 0.8 μm dataset. (g) Computed F-scores (blue dots) as a function of focal spot spacing, and a smoothing spline fit (black line) that serves as a guide to the eye. The shaded region indicates one standard deviation from the mean F-score. (h) A comparison of the x-shifts and y-shifts retrieved with the motion correction algorithm for 0.8 μm sampling (blue) and 4 μm sampling (dark blue), and the difference between them (black dashed line). The 4 μm sampling shifts are upsampled and vertically offset for ease of comparison.

Additionally, we studied whether optimizing spatial sampling affects motion correction. For this analysis the dataset was denoised and filtered, and then points were removed to create additional time series with gradually increasing focal spot spacing as above. We then ran our usual motion correction algorithm on the datasets and compared the retrieved motion in the x and y axes. The x shifts and y shifts of 0.8 μm spacing and 4 μm spacing were identical (Supplementary Fig. 1h; 4 μm traces are upsampled and vertically offset by 3 pixels for clarity), indicating that motion correction is generally not affected by sampling optimization.

1.2 Optimizing the temporal sampling rate

Similarly, the desirable frame rate for 3P calcium imaging with GCaMP6s is the minimum frame rate that allows to resolve calcium events. In order to find that frame rate, we performed a similar study of how the frame rate affects event extraction. First, we recorded a time series of neuronal activity in a mouse hippocampus labeled with GCaMP6s, with a 27 Hz frame rate. The dataset was denoised, motion-corrected and filtered to remove galvo-related artifacts. Then frames were removed to create additional time series with a gradually decreasing frame rate, from 16 Hz to 0.25 Hz (Supplementary Fig. 2a-c). Those time series were upsampled back to the native frame rate for comparison. All the resulting time series were then deconvolved to extract events using OASIS [2]. The extracted event sequences were compared against those retrieved from the 27 Hz dataset, by computing the cosine similarity between the matrix of extracted events from all cells for the low frame rate dataset and the matrix of extracted events from all cells for the 27 Hz dataset. An event was considered detected if its timing was correct to within 0.2 s, half the rise time of GCaMP6s. The variance was computed by splitting the FOV of the original dataset into five and running this analysis pipeline on each of those datasets. The resulting plot shows an increasing similarity with increasing frame rate, with a minimal drop, from 1 to approximately 0.9, between 27 Hz and 6 Hz (Supplementary Fig. 2d; error bars represent one standard deviation from the mean cosine similarity). We therefore chose 6 Hz as the design frame rate for LIFT.

1.3 A general framework for sampling optimization

While the focus of this work is on calcium imaging of neuronal somata with GCaMP6s, the versatility of LIFT scope allows optimization of spatial and temporal sampling rates for a wide range of applications. The most accurate method of determining the optimal sampling rate for a particular structure and indicator is to run tests on the acquired data, as detailed in sections 1.1 and 1.2 above, and choose the minimal sampling rates that yield the desired structure and event segmentation fidelities. As a general rule of thumb, the sampling rate should follow the Nyquist criterion, i.e. it should always exceed twice the maximal spatial or temporal frequency to be resolved. That is, if the structure to be resolved is of size x_0, that would correspond to spatial frequency $k_0 = 2\pi/x_0$. The sampling frequency, $k_f = 2\pi/x_f$, where x_f is the distance between focal spots, should therefore follow:

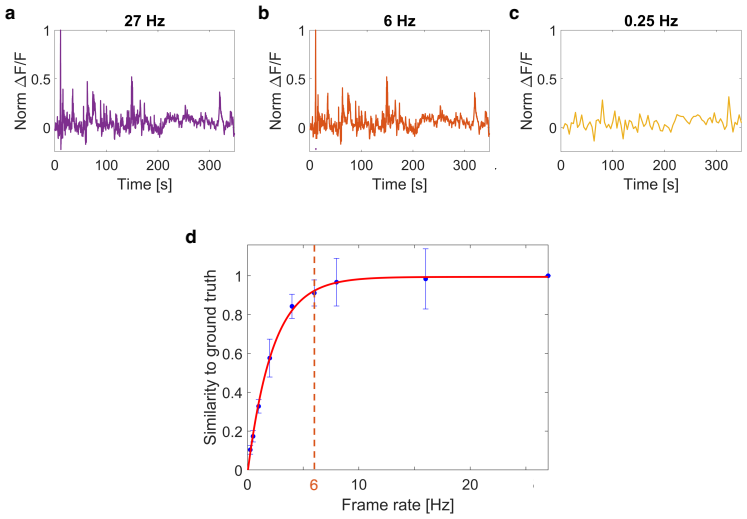
$$k_f > 2k_0 \tag{1}$$

Therefore x_f, the distance between focal spots, should follow:

$$x_f < x_0/2 \tag{2}$$

Similarly, if the temporal event to be resolved is of duration t_0, the frame rate f_{frame} should follow:

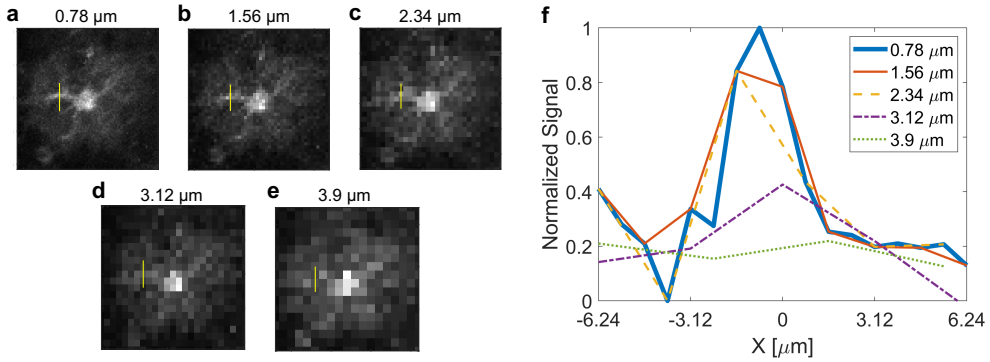
$$f_{frame} > 2f_0 \tag{3}$$



Supplementary Fig. 2 The fidelity of calcium event extraction as a function of frame rate. (a) An example trace recorded at a frame rate of 27 Hz. (b) The same trace as in a, downsampled to 6 Hz. (c) The same trace as in a, downsampled to 0.25 Hz. (d) Computed cosine similarities (blue dots) between the calcium events extracted from a dataset recorded at 27 Hz and temporally downsampled datasets, and an exponential fit (red line) to guide the eye. The error bars represent one standard deviation from the mean cosine similarity. The similarity between the calcium events extracted from the 27 Hz dataset and the calcium events extracted from the 6 Hz dataset, the design frame rate of LIFT, is > 0.9.

where $f_0 = 1/t_0$ is the minimal temporal frequency to be resolved. For calcium imaging, t_0 is typically taken to be the rise time. For GCaMP6s, the rise time is approximately 0.4 s, which dictates a frame rate greater than 5 Hz.

As an example of how these rules apply generally, we show how the spatial sampling rule (Eq. 2) can be applied to imaging of astrocytic processes. Several processes are visible in a raw 3P image of cortical astrocytes acquired with 0.78 μm focal spot spacing (Supplementary Fig. 3a). The intensity profile along the yellow line, extending through the most visible process, yields a full width at half maximum of 3.4 μm when fitted to a Gaussian (Supplementary Fig. 3f; solid blue line). Images of the same FOV with increased focal spot spacing were generated by removing data points as in section 1.1 (Supplementary Fig. 3b-e). Following Eq. 2 above, the focal spot spacing should not exceed $3.4/2 = 1.7$ μm. We can see that in fact, while a focal spot spacing of 1.56 μm correctly resolves the location and width of the process (Supplementary Fig. 3f; solid orange line), a focal spot spacing of 2.34 μm begins to underresolve the process, leading to some error in the location (Supplementary Fig. 3f; dashed yellow line). Further increasing the focal spot spacing to 3.12 μm (Supplementary Fig. 3f; dot-dashed purple line) increases error in location and width and reduces the SNR until the process can no longer be resolved at all at 3.9 μm focal spot spacing (Supplementary Fig. 3f; green dotted line). To achieve a 1.56 μm focal spot spacing with LIFT, the



Supplementary Fig. 3 The effect of focal spot spacing on the imaging of astrocytic processes. (a) An unprocessed three-photon image of a cortical astrocyte in mouse brain, acquired with 0.78 μm focal spot spacing. (b)-(e) The same image as in a, with focal spot spacings of 1.56 μm, 2.34 μm, 3.12 μm, and 3.9 μm, respectively. (f) The intensity profiles along the yellow lines in a-e.

FOV or frame rate can be adjusted. One example parameter set is 1.56 μm focal spot spacing, 6 Hz frame rate, 650 x 650 μm FOV.

Supplementary Note 2: Imaging improvement due to sampling optimization

Since tissue heating restricts the excitation power in 3P microscopy, optimized spatial and temporal sampling increases the SNR of calcium imaging data compared to conventional sampling for *any* FOV size, for two reasons. First, optimized spatial sampling allows to reduce the repetition rate of the source (or number of beamlets if using spatiotemporal multiplexing) because it uses fewer focal spots to sample the FOV and therefore requires a lower data acquisition rate. Similarly, optimized temporal sampling requires a lower acquisition rate because it uses fewer frames to sample an event. Reducing the repetition rate or beamlet number allows, in turn, for higher excitation pulse energies for the same excitation power. Due to the highly nonlinear dependence of the signal on pulse energy, higher pulse energies result in higher SNR, as explained below.

Secondly, with optimized spatial sampling, the excitation power can be increased beyond the levels used for small FOV imaging with conventional sampling, as the lower density of heat sources helps mitigate tissue heating. This further increases pulse energy and SNR. Overall, the SNR gain from sampling optimization can be utilized to improve FOV size, increase frame rate, or extend imaging depth.

When recording activity from a cell with a shot-noise-limited system, the SNR of the recorded fluorescence trace scales with the number of spatial samples, N_c, within the cell body and the signal power per pixel, S_{pp}:

$$SNR \propto \sqrt{N_c S_{pp}} \tag{4}$$

For a single pulse per pixel measurement, the signal power per pixel depends on the energy of the pulse as $S_{pp} \propto {E_P}^3$, where E_P is the pulse energy, and the pulse duration is fixed. Substituting that into 4 gives:

$$SNR \propto \sqrt{N_c {E_P}^3} \tag{5}$$

N_c, the number of spatial samples that fall within one cell, can be expressed as $N_c = A_c f_x^2$, where A_c is the cell area, and $f_x = 1/x$ is the spatial sampling frequency, with x being the distance between focal spots. For a given FOV size, the maximal f_x possible depends on the frame rate, f_{frame}, and the repetition rate, f_{rep}, of the excitation source, assuming a single-pulse-per-pixel measurement:

$$N_c \propto f_x^2 \propto \frac{f_{rep}}{f_{frame}} = \frac{P_{exc}}{f_{frame} E_p} \tag{6}$$

Where P_{exc} is the excitation power of the source, and $P_{exc} = E_P f_{rep}$. Since typically 3P systems use the maximum power that has been shown not to cause overheating for a given imaging depth, we will assume $P_{exc} = P_{max}$. Substituting $E_P \propto \frac{P_{max}}{N_c f_{frame}}$,

into 5 gives:

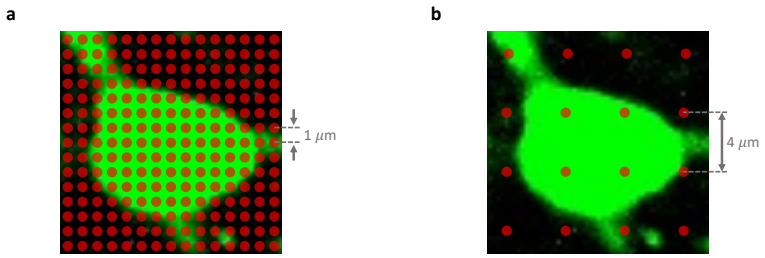
$$SNR \propto \frac{1}{N_c} \left(\frac{P_{max}}{f_{frame}} \right)^{\frac{3}{2}} \tag{7}$$

Expressing this in terms of the spatial sampling frequency, f_x, gives:

$$SNR \propto \frac{1}{f_x^2} \left(\frac{P_{max}}{f_{frame}} \right)^{\frac{3}{2}} \tag{8}$$

Therefore, in principle the optimal sampling of a cell for a given excitation power is with a single spatial sample (N_c=1, $f_x \to 0$) and a single temporal sample ($f_{frame} \to 0$), as evident from Fig. 1i. Yet in practice there are several limitations. First, recording activity from cells labeled by an indicator requires a minimal frame rate in order to resolve that indicator's kinetics. For GCaMP6s, our data (Supplementary Note 1.2, Supplementary Fig. 2) shows that 6 Hz is the lowest frame rate that allows to maintain high calcium event extraction fidelity. Second, the number of spatial samples of a cell must yield the necessary spatial resolution to resolve it. For cells with an average diameter of 10 - 15 μm, our data (Supplementary Note 1.1, Supplementary Fig. 1) shows that 4 - 5 μm focal spot spacing is the largest spacing that preserves cell segmentation fidelity. We chose the average sampling distance to be 4 μm to account for the variation in focal spot spacing due to the nonlinearity of the scan (see Supplementary Fig. 13). In conventional 3P microscopy, focal spots are spaced by 0.5 - 1 μm. Using 1 μm sampling (Supplementary Fig. 4a) a 9 x 11 μm cell is sampled by 70 - 80 focal spots, whereas in LIFT microscopy (Supplementary Fig. 4b) it is sampled by 4 - 6 pixels. Consequently, the SNR of recorded fluorescence traces using LIFT microscopy is $\sim$10 times higher than the SNR using 1 μm sampling of the same FOV, regardless of FOV size. The increase in SNR due to the use of optimized sampling allows to image deeper into the brain. Conversely, to achieve high enough SNR to image large FOVs at a 1 mm depth, conventional sampling schemes [3] would have to use an excitation power 10x higher than P_{max}, resulting in heating damage. Equations 4 - 8 can also be expressed in terms of the 3P signal, S, and the number of focal spots per line, N, to yield: $S \propto E_p^3 = (\frac{P_{max}}{f_{rep}})^3 \propto \frac{1}{N^6}$ (see Fig. 1d).

Moreover, due to the reduced density of heat sources, the excitation power in LIFT microscopy can be increased relative to the established maximum safe powers for conventional small FOV microscopy. To our knowledge, the safety of excitation powers in 3P microscopy has been assessed with a 0.5 μm sampling scheme over a 230 x 230 μm FOV [4]. Under those conditions, the maximum excitation power that was found to be safe was $\sim$1 mW at the focal plane, for a depth of $\sim$1 mm. Optimized spatial sampling enables higher excitation powers because the heat sources are spread over a larger area. Since the frame rates compatible with calcium imaging are fast enough to neglect tissue cooling between successive frames ($\sim$0.1°C/s) [4, 5], brain heating can be modeled as under continuous illumination of the focal spots of all the pixels in the FOV. Under those conditions, the total resulting temperature distribution is the sum of the temperature distributions from each focal spot, due to the linearity of the diffusion equation. As each focal spot will create a temperature increase over

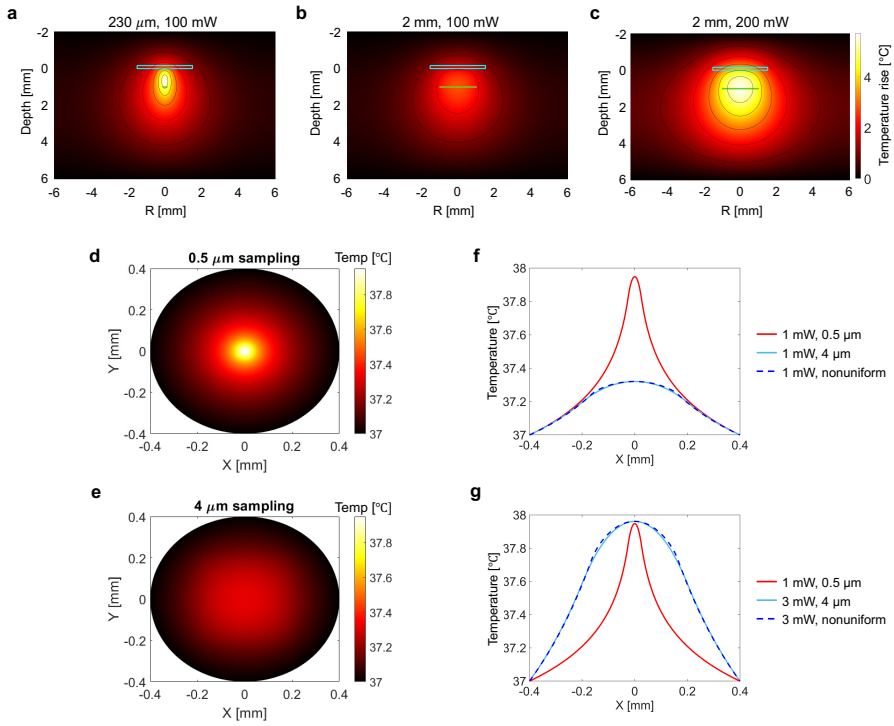


Supplementary Fig. 4 A comparison of the sampling schemes used in conventional microscopy and LIFT. (a) An example of a conventional sampling scheme, with a 0.7 μm point-spread function (PSF) and 1 μm focal spot spacing. A cell is sampled by 70 - 80 focal spots. (b) A schematic of the optimized sampling scheme used by LIFT, with a 0.7 μm PSF and 4 μm focal spot spacing. A cell is sampled by 4 - 6 focal spots.

a certain local volume, the closer the focal spots are to each other, the more these volumes overlap. As a result, the total local temperature rise is lower for larger focal spot separations.

To study the reduction in heating due to optimized sampling quantitatively, we numerically modeled the heating from a small FOV with 0.5 μm sampling and a large FOV with 4 μm sampling. Due to the high computational cost of a simulation with a spatial resolution that allows to resolve individual PSFs while simulating a centimeter-scale 3D volume, we performed two different numerical studies. The first was adapted from Wang *et al.* [4] and previous work [1, 5], and simulated the entire volume (a cylinder of radius 6 mm and height 8 mm, as in [4]) but with spatially homogeneous illumination over the entire FOV instead of individual Gaussian focal spots separated by the focal spot spacing. Brain heating was assessed using a Monte Carlo simulation to find the distribution of light scattered and absorbed, and then the finite difference method was used to evaluate the heating profile. We found that the brain heated more for a 230 μm FOV diameter (Supplementary Fig. 5a) than for a 2 mm FOV diameter (Supplementary Fig. 5b), and that the excitation power could be increased by a factor of 2 for a 2 mm FOV diameter relative to the power for a 230 μm FOV diameter, while maintaining the same maximum temperature (Supplementary Fig. 5c).

In another simulation, we studied the heating at the focal plane from individual focal spots that were either spaced by 0.5 μm or 4 μm (Supplementary Fig. 5d-g). The simulation had a 2D circular geometry, and the simulated window extended to r = 400 μm, which was the maximum window size possible computationally with the resolution necessary to resolve the individual PSFs. We used a square array of 100 x 100 focal spots, and the temperature was fixed at 37°C at the simulated window boundary. In agreement with the homogeneous illumination simulation, the brain heated more for 0.5 μm focal spot spacing (Supplementary Fig. 5d) than for 4 μm focal spot spacing (Supplementary Fig. 5e) for 1 mW of power at the focal plane (Supplementary Fig. 5f). To verify that the nonuniformity in focal spot spacing introduced by the galvanometer scan pattern does not substantially affect heating, we also simulated



Supplementary Fig. 5 Heating simulation results. The temperature distribution resulting from imaging at a 1 mm depth with 1300 nm light in mouse brain, using spatially homogeneous illumination over an area of diameter (a) 230 μm and 100 mW of power, (b) 2 mm and 100 mW of power, and (c) 2 mm and 200 mW of power. R represents the distance (radius) from the center of the FOV and the color scale represents the increase in temperature during the imaging time and is the same for a-c. All powers are post objective. The green line indicates the scan area. The temperature distribution in the focal plane, resulting from continuous scanning of 100 x 100 focal spots with 1300 nm light and (d) 1 mW of excitation power with 0.5 μm sampling, and (e) 1 mW of excitation power with 4 μm sampling. (f) A comparison of the temperature distributions resulting from 1 mW excitation with 0.5 μm sampling, 4 μm uniform sampling, and 4 μm nonuniform sampling, in the center of the focal plane (y=0). (g) A comparison of the temperature distributions resulting from 1 mW excitation with 0.5 μm sampling, 3 mW excitation power with 4 μm uniform sampling, and 3 mW excitation power with 4 μm nonuniform sampling, in the center of the focal plane, showing that the maximum temperature in all three cases is similar.

the heating from focal spots spaced according to LIFT's scan waveform (Supplementary Fig. 13). The uniform (Supplementary Fig. 5f; solid cyan line) and nonuniform (Supplementary Fig. 5f; dashed blue line) cases yielded very similar results, with the nonuniform case showing slightly increased heating at the edge of the FOV but no increase in the maximal temperature. In this simulation, the excitation power could be increased by a factor of 3 for 4 μm focal spot spacing (uniform and nonuniform)

relative to 0.5 μm focal spot spacing, while maintaining the same maximum temperature (Supplementary Fig. 5g). The possible power increase for 4 μm sampling could be larger in this simulation because it accounts for the reduced overlap between the heating profiles caused by individual focal spots and not just the reduced power density, which the homogeneous illumination simulation (Supplementary Fig. 5a-c) accounts for. The gain in SNR from increasing the excitation power can be utilized to improve imaging depth, or frame rate/FOV size by increasing the repetition rate.

Supplementary Note 3: The challenges in using conventional beam scanning mechanisms in large FOV 3P imaging

As multiphoton microscopy is typically used to image inside scattering samples, spatial features cannot be resolved from a wide-field image of the emitted fluorescence. Rather, spatial resolution is typically achieved by focusing the excitation light to a point and scanning the focus point by point over the sample plane. For each point, all the emitted fluorescence is collected and sent to a bucket detector, and the image is the composite two-dimensional array of detected intensities. In order to scan the beam, various scanning mechanisms are commonly used: a galvanometer, a resonant galvanometer, a polygon scanner, and a micro-electro-mechanical system (MEMS) scanning mirror.

A galvanometer is the most commonly used beam scanning device. It allows for flexibility in the choice of scan speed, scan angle and scan waveform (i.e. the user can control the position of each individual scan point on the sample). Galvanometers have relatively large optical apertures and allow large-angle scanning, albeit at compromised speeds. When using off-the-shelf optics, the beam is typically magnified from the galvanometer to the back aperture of the objective by a factor of ~ 4. With this geometry and a 1 MHz repetition rate, a high-performance galvanometer can scan at about half the required speed for 4 μm sampling.

A resonant galvanometer is typically used for applications that require high-speed scanning. Large aperture resonant scanners can scan large angles at frequencies of several kHz. However, resonant scanners can typically scan only at their resonant frequency and only with a sinusoidal waveform. This property has two drawbacks: since the scan speed is set, so is the frame rate. Therefore, in one-pulse-per-pixel imaging, the user can only choose pairs of FOVs and focal spot spacings that result in that frame rate. Furthermore, the sinusoidal scan pattern results in large focal spot spacing in the center of the FOV and small focal spot spacing at the edges. For a 2-mm-diameter FOV, a sinusoidal scan pattern that provides the desired frame rate of 6 Hz would result in a focal spot spacing of > 6 μm at the center of the FOV. Finally, resonant scanner frequency can vary based on the particular mirror geometry and often cannot be controlled to provide the exact desired frequency and thus the desired focal spot spacing.

A polygon scanner can scan large angles with large optical apertures, and its scan speed can be tuned. Since beam scanning is based on rotation of the polygon, it is the only scanner that does not oscillate back and forth and therefore is the only scanner that can provide a completely linear scan and uniform sampling. However, the scan angle cannot be varied and thus neither can the FOV. Furthermore, polygon scanners with optical apertures that are large enough to fill the back aperture of a typical objective with a 4x magnification as described above require very large scan angles. These scan angles typically require specially designed, bulky scan lenses. Finally, polygon scanners suffer from pupil shifting due to the shifting of the location of the reflection point from the scanner facet during rotation.

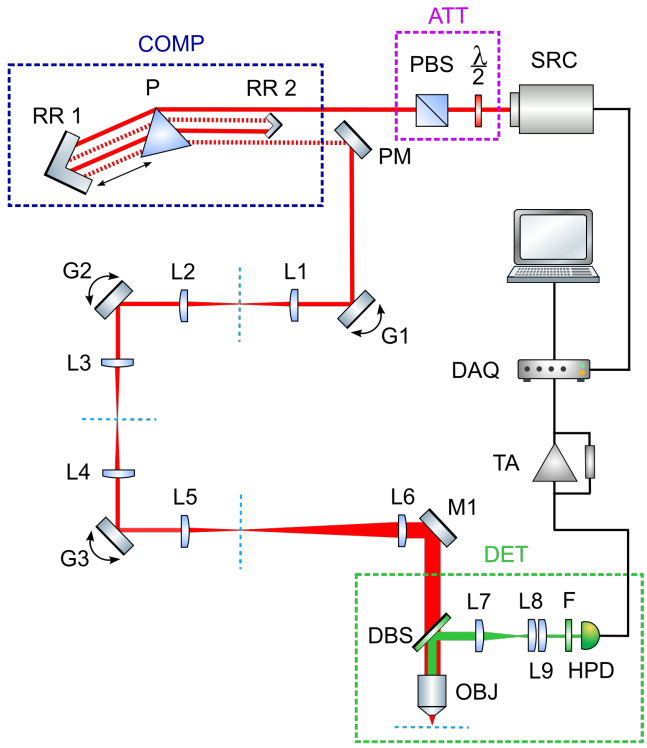
A MEMS scanner allows for both large scan angles and large scan speeds, and provides the ability to tailor the scan waveform. Yet currently MEMS scanners that support those scan speeds and angles have relatively small optical apertures. Using such apertures would either result in significant underfilling of the objective back aperture, or in a reduction of the scanned FOV due to a magnification larger than 4x.

Our custom scanning module overcomes all of these challenges by using a galvanometer relay, as shown in Fig. 2a. The use of a galvanometer relay doubles the scan speed of a galvanometer while preserving all of its advantages, allowing the user to choose any combination of frame rate, focal spot spacing and FOV possible given the laser repetition rate. The scan waveform can be tailored for large FOV calcium imaging so that the focal spot spacing in the FOV center does not significantly exceed 5 μm, yet the overall scan frequency results in the desired frame rates. Furthermore, our scanner enables random access scanning, which is used in a variety of applications, such as targeted illumination microscopy [6] and patterned optogenetic stimulation [7]. Finally, our scanner can be easily replicated, using all off-the-shelf components.

Supplementary Fig. 6: Detailed system schematic

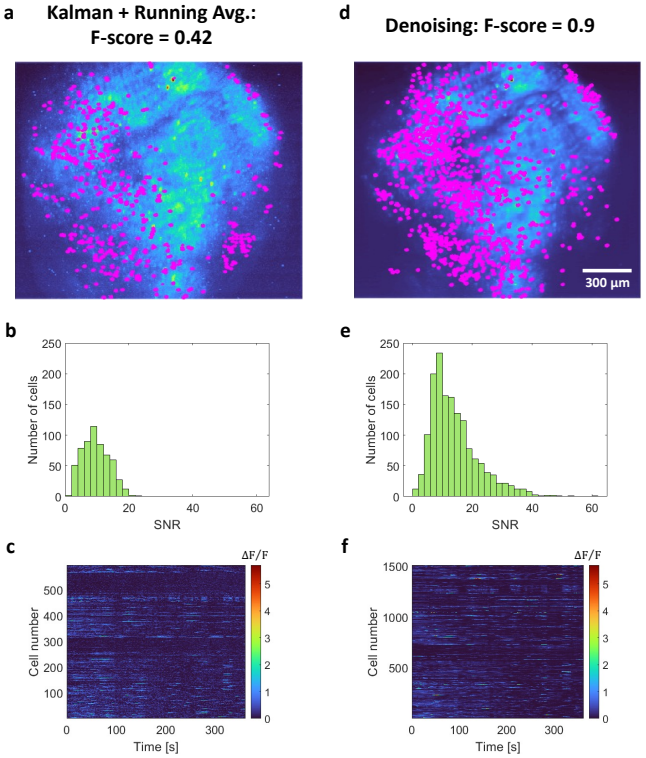
SRC	Excitation source
λ/2	Half-wave plate
PBS	Polarizing beam splitter
P	Prism
RR	Retroreflector
PM	Pick-off mirror
G	Galvanometer scanner
L	Lens
OBJ	Objective
DBS	Dichroic bean splitter
F	Bandpass Filter
HPD	Hybrid photodetector
TA	Transimpedance amplifier
DAQ	Data acquisition system
ATT	Variable attenuator
COMP	Prism compressor
DET	Detection module

Element pair	Distance [mm]
P-RR1	Variable
P-RR2	122
G1-L1	54
L1-L2	108
L2-G2	54
G2-L3	54
L3-L4	108
L4-G3	54
G3-L5	54
L5-L6	254
L6-OBJ	200
L7-L8	109
L8-L9	1.5
L9-HPD	11



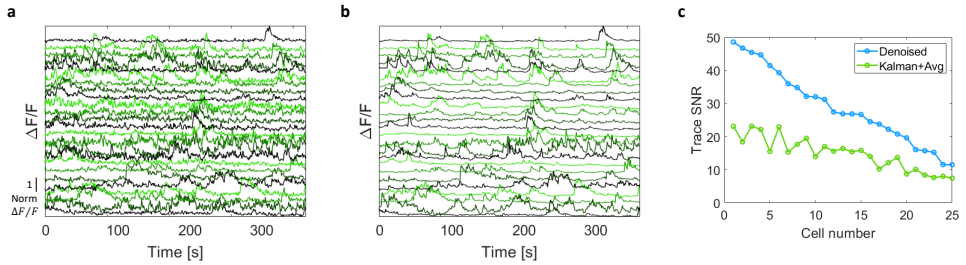
A detailed schematic of the experimental setup. ATT = variable power attenuator, COMP = single prism pulse compressor, DET = detection module. See Supplementary Table 2 for component list. Dotted beam paths are elevated above the solid paths (RR2 translated the beam upward [8]).

Supplementary Fig. 7: A comparison of denoising and filtering for postprocessing of datasets



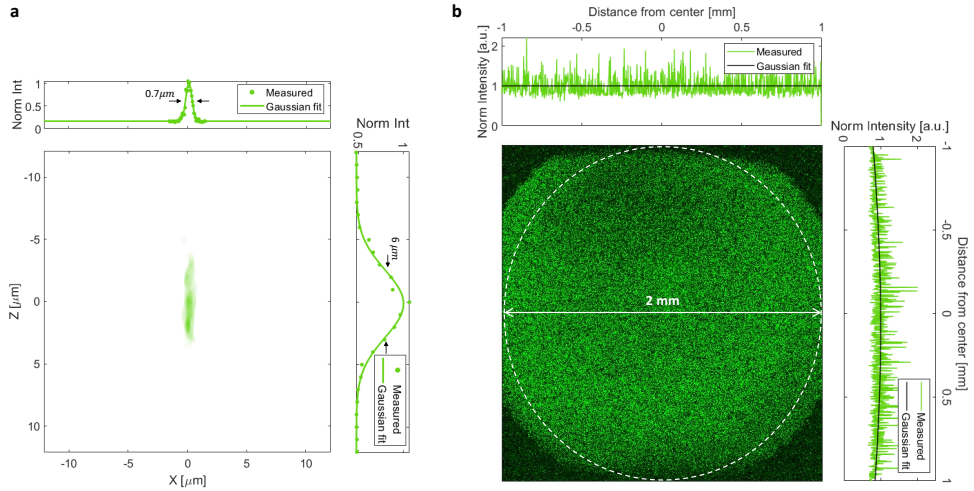
A comparison of the dataset analyzed in Fig. 5a-e, processed by filtering (a-c) and processed by denoising (d-f). (a) The maximum intensity projection of the filtered time series, and the contours of 570 active cells plotted in magenta on top. The data was processed using our data processing pipeline, yet instead of denoising, the time series was filtered with a Kalman filter with 0.75 gain and then smoothed with a temporal running average of length 6. The fidelity of cell segmentation, evaluated using the F-score (see Supplementary Note 1), was low (F-score = 0.42). (b) A histogram of the SNRs of the extracted activity traces. For the comparison, the noise was defined as the standard deviation of the top 20% of frequencies and the signal was defined as in the main text. (c) The full dataset, including traces from all active cells. The color scale corresponds to the normalized $\Delta F/F$ value. (d)-(f) The same as a-c, but for the denoised data. The number of cells detected in the denoised data is nearly triple the number detected in the filtered data, and the fidelity of cell segmentation is more than double (F-score = 0.9). For a direct comparison of the extracted traces, see Supplementary Fig. 8.

Supplementary Fig. 8: A comparison of traces from denoised data and filtered data



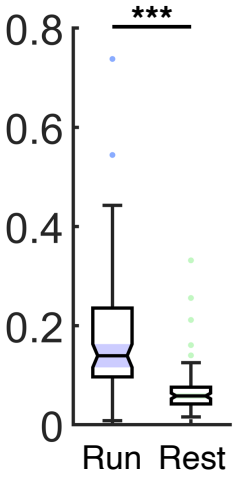
(a) Traces retrieved from 25 example ROIs from the data presented in Supplementary Fig. 7a-c, which was filtered with a Kalman filter with 0.75 gain and then smoothed with a temporal running average of length 6. (b) Traces retrieved from the same ROIs as in panel a, but from the denoised dataset, presented in Supplementary Fig. 7d-f. (c) A comparison of the SNRs of the traces in a and b. The cells are numbered according to their order in panels a-b, with Cell 1 being the top trace. The SNR was defined as in Supplementary Fig. 7. Overall, the SNR of the denoised data is higher while the calcium events are preserved.

Supplementary Fig. 9: The point spread function of LIFT scope and the uniformity over its field of view



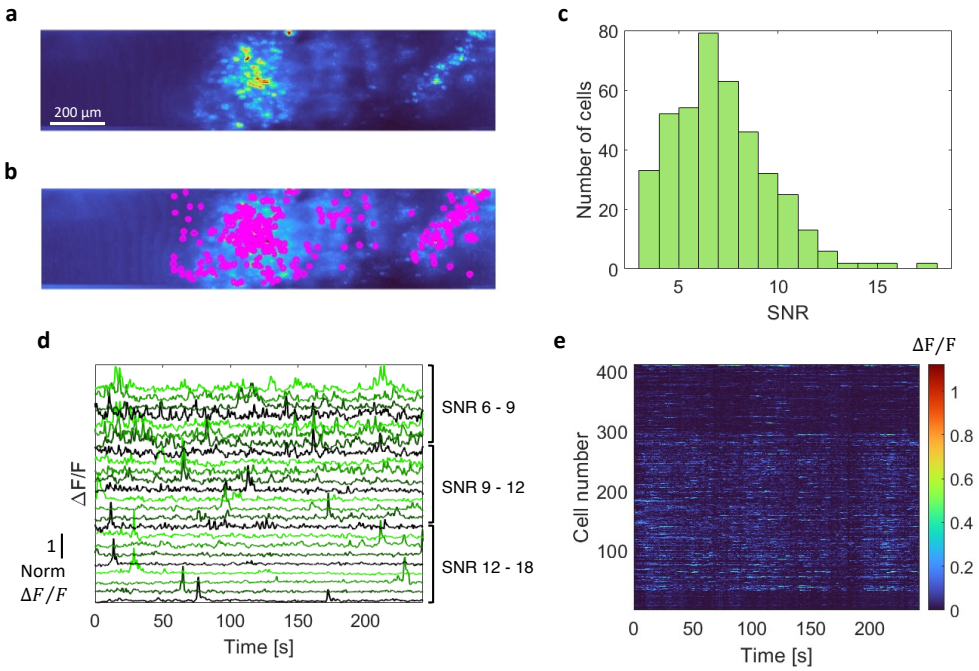
(a) The 3P point spread function (PSF) of LIFT scope, measured on 0.5 μm fluorescent beads. Top: The intensity profile of the measured lateral PSF (green dots) and a Gaussian fit with a FWHM of 0.7 μm (green line). Right: The intensity profile of the measured axial PSF (green dots) and a Gaussian fit with a FWHM of 6 μm (green line). Some waviness is noticeable in the z-axis of the PSF image, due to a slight wobble in the mechanical scan. The axial width is larger than the diffraction-limited width due to spherical aberrations arising from the use of a coverslip with an objective that does not include a correction collar. This configuration is consistent with our in vivo imaging preparation, in which a coverslip of the same thickness is used as an optical window. (b) The measured 3P signal from a uniform sample (fluorescein solution) over the FOV of LIFT scope (raw image, no averaging or denoising used). The white dashed circle represents LIFT's full, 2-mm-diameter FOV. Top: The intensity profile across a horizontal line through the center (green line) and a Gaussian fit (black line). Right: The intensity profile across a vertical line through the center (green line) and a Gaussian fit (black line).

Supplementary Fig. 10: Statistical analysis of run versus rest neuronal activity



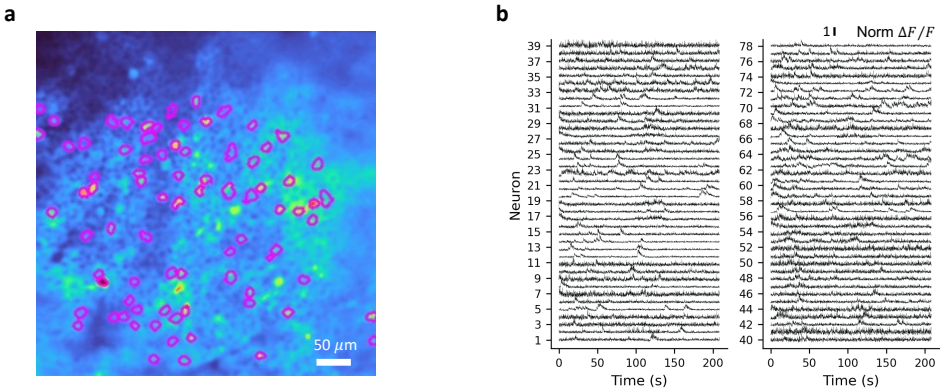
Comparison of $\Delta F/F$ per cell during rest and run periods (pairwise two-sided Wilcoxon signed-rank test; $n = 86$ cells; $P = 3 \times 10^{-15}$). Box plots: box, 25th (Q1, bottom line) to 75th (Q3, top line) percentiles; whiskers, $Q1 - 1.5 \times IQR$ to $Q3 + 1.5 \times IQR$, where $IQR = Q3$–$Q1$; middle line, median (m); notch, from $m + (1.57 \times IQR)/\sqrt{n}$ to $m - (1.57 \times IQR)/\sqrt{n}$; dots, measurement points.

Supplementary Fig. 11: 3P population imaging in the mouse hippocampus at video rate



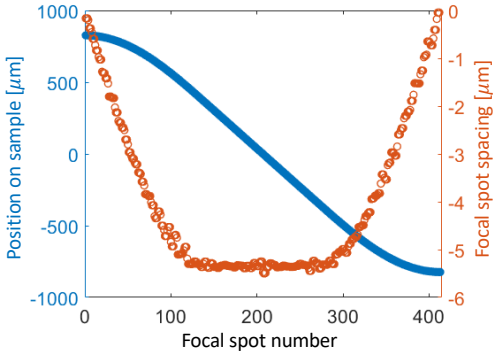
Neuronal activity recording at a 27 Hz frame rate, over a 0.73 mm^2 FOV, at a depth of 1005 μm in the mouse hippocampus. (a) The maximum intensity projection of the time series. (b) Contours of 400 active cells, plotted in magenta, on top of the MIP. (c) A histogram of the SNRs of the extracted activity traces shows that the majority of cells have $3 < \text{SNR} < 8$. (d) Examples of traces from various SNR ranges. (e) The full dataset, including traces from all active cells. Imaging was performed with 4 μm lateral sampling and cells were labeled with GCaMP6s.

Supplementary Fig. 12: High-resolution 3P calcium imaging in the mouse hippocampus



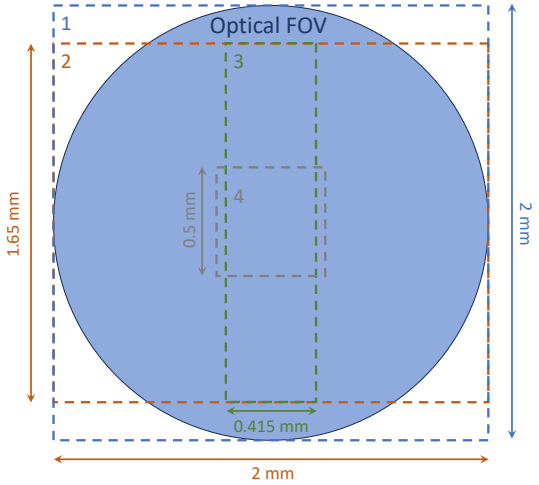
Neuronal activity recording with 2 μm lateral sampling at a 11 Hz frame rate, over a 500 x 500 μm FOV, at a depth of 948 μm in the mouse hippocampus. The data was motion corrected and artifacts were removed but it was not denoised or filtered. (a) The mean intensity projection of the recorded time series. Contours of active cells segmented using our CNMF-based software are plotted on top in magenta. (b) The corresponding activity traces, normalized to the maximum value of the trace.

Supplementary Fig. 13: Scan waveform and focal spot spacing



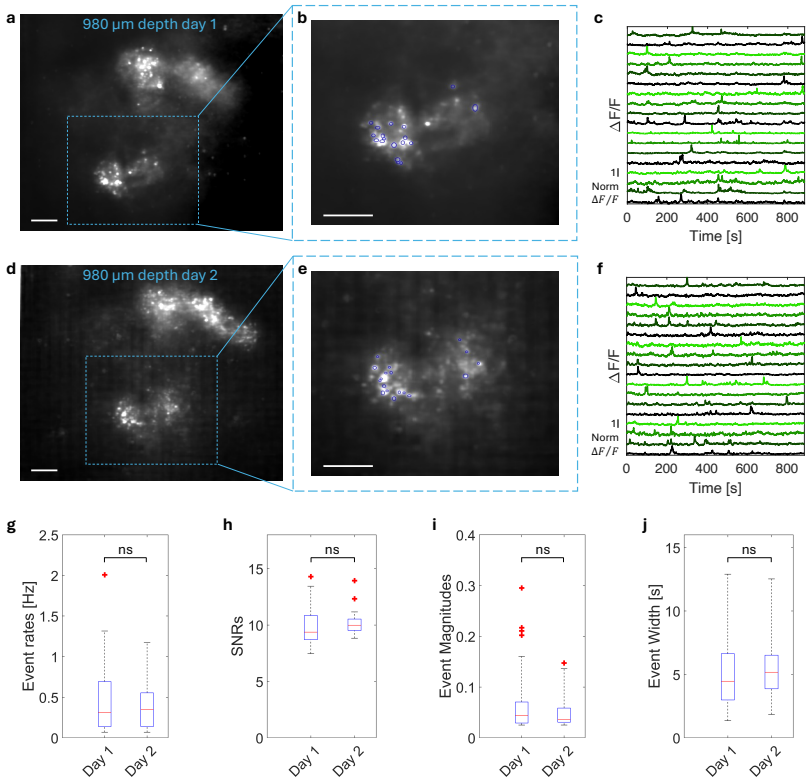
The lateral position of the beam in the fast axis of the sample plane as a function of focal spot number (or time), for the waveform used for a 3 mm^2 FOV scan at a 6 Hz frame rate (blue circles), and the corresponding spacing between adjacent focal spots (orange circles). Beam positions were determined from the x-galvo drive voltages using an empirical FOV calibration from grid-slide images. The drive-voltage limits were mapped to the measured FOV boundaries. The computed beam positions were validated by unwarping distorted grid images and recovering the expected regular grid geometry.

Supplementary Fig. 14: Field of view geometry



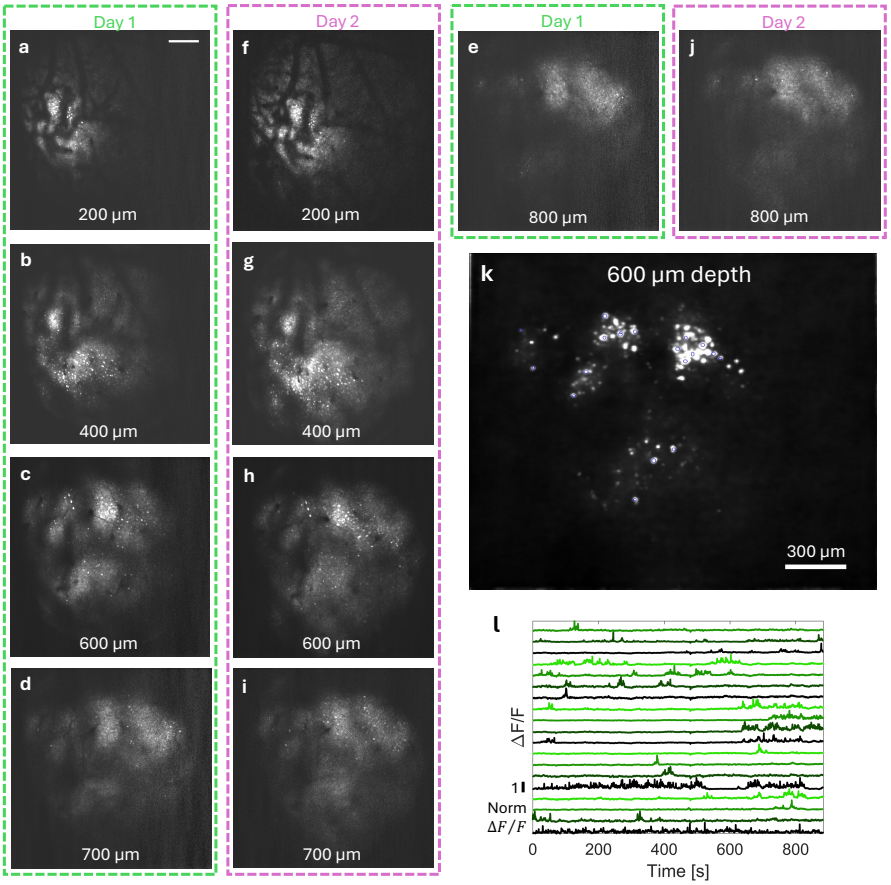
A schematic showing the scanned FOV for the datasets shown in this work. 1 - Scanned FOV for high-resolution structural imaging, presented in Figs. 3 and 6. 2 - Scanned FOV for 6 Hz calcium imaging, presented in Figs. 4 and 5. 3 - Scanned FOV for video-rate calcium imaging, presented in Supplementary Fig. 11. 4 - Scanned FOV for high-resolution 10 Hz calcium imaging, presented in Supplementary Fig. 12.

Supplementary Fig. 15: A rescan of a neuronal population in the mouse hippocampus



(a) The maximum intensity projection of a time series recorded at 980 μm depth in an awake mouse on day 1, with 124 mW post-objective power. Scale bar, 200 μm. (b) A zoom-in on CA1, with blue ROIs plotted on top. Scale bar, 400 μm. (c) Calcium activity traces acquired from the ROIs in b. Traces are vertically offset and colored for clarity. (d)-(f) Same as a-c, acquired in the same animal the following day. (g) A comparison of the event rate in the traces in c and f (pairwise two-sided Wilcoxon signed-rank test; $n = 18$ cells; $P = 0.5$). Box plots: box, 25th (Q1, bottom line) to 75th (Q3, top line) percentiles; whiskers, $1.5 \times IQR$, where $IQR = Q3–Q1$; middle line, median. (h) Same analysis as g, for the signal-to-noise ratio of the traces ($P = 0.25$). (i) A comparison of the event magnitudes ($\Delta F/F$) in the traces (two-sided Wilcoxon rank sum test; $n_1 = 135$, $n_2 = 99$; $P = 0.37$). Box plots: box, 25th (Q1, bottom line) to 75th (Q3, top line) percentiles; whiskers, $3 \times IQR$, where $IQR = Q3–Q1$; middle line, median. (j) Same analysis as i, for the event width ($P = 0.12$). All tests show the differences between the traces from days 1 and 2 are not significant (ns), indicating that the tissue was not altered by imaging.

Supplementary Fig. 16: Structural and functional imaging of brain areas dorsal to the rescanned neuronal population



Structural and functional imaging performed in the same animal as in Supplementary Fig. 15, in the brain regions dorsal to the scanned area at 980 μm depth. High-resolution structural images acquired on day 1 prior to scanning, at depths (a) 200 μm, (b) 400 μm, (c) 600 μm, (d) 700 μm, and (e) 800 μm. (f)-(j) Same as a-e, but acquired on day 2. No signs of damage are observed. Minor differences between images acquired at the same depth arise from slight variations in imaging location and animal head tilt between the two days, as well as from variability in cellular activity during image acquisition. (k) The maximum intensity projection of a time series acquired on day 2 at 600 μm depth with ROIs plotted in blue on top. (l) The calcium activity traces retrieved from the ROIs in k, showing normal activity patterns. These results indicate that imaging did not alter the tissue dorsal to the scanned region.

Supplementary Table 1: Comparison of LIFT to other 3P systems capable of performing calcium imaging at 1 mm depth

	FOV size [mm²]	Lateral PSF size [µm]	Focal spot distance [µm]	Frame rate [Hz]	Animal mobility
LIFT large FOV mode	3.1	0.7	4	5.8	Head-fixed
LIFT video-rate mode	0.73	0.7	4	26.8	Head-fixed
LIFT high-resolution video-rate mode	0.02	0.7	0.78	27	Head-fixed
LIFT intermediate mode	0.28	0.7	1.95	9.65	Head-fixed
Ref. 25, Klioutchnikov et al. 2020	0.019	0.8	1.16	27.8	Head-mounted
Ref. 29, Ouzounov et al. 2017	0.04	N/A	0.78	8.5	Head-fixed
Ref. 30, Weisenburger et al. 2019	0.115	1.5	3.4	78	Head-fixed
Ref. 31, Zhao et al. 2023	0.0625	1	1	8.35	Head-mounted
Ref. 34, Mok et al. 2024	0.295	0.7	1.06	4.3	Head-fixed

Specifications for all 3P imaging modalities compared in Fig. 2c of the main text

Supplementary Table 2: Component list for LIFT

	Vendor	Part number	Qty	Description and link
SRC	Coherent	Opera-F	1	Optical Parametric Amplifier for Yb Systems https://www.coherent.com/resources/datasheet/lasers/opera-f-ds.pdf
HWP	Thorlabs	AHWP10M-1600	1	Ø1" Mounted Quartz Zero-Order Achromatic Half-Wave Plate, SM1-Threaded Mount, 1100 - 2000 nm
PBS	Thorlabs	CCM1-PBS254	1	30 mm Cage Cube-Mounted Polarizing Beamsplitter Cube, 1200-1600 nm, 8-32 Tap https://www.thorlabs.com/thorproduct.cfm?partnumber=CCM1-PBS254
P	Edmund	49-432	1	50mm N-SF11 Uncoated Equilateral Prism https://www.edmundoptics.com/p/50mm-n-sf11-uncoated-equilateral-prism/9863/?srsltid=AfmBOopw3pzrE75CfECjQqlDhnuMjOU_x-gfWgLRqrEhVbd-t-PZYa9F
RR1, RR2	Thorlabs	HRS1015-P01	2	1" x 1" Hollow Roof Prism Mirror, Protected Silver https://www.thorlabs.com/thorproduct.cfm?partnumber=HRS1015-P01
PM	Thorlabs	PFD10-03-P01	1	Ø1" Protected Silver D-Shaped Mirror https://www.thorlabs.com/thorproduct.cfm?partnumber=PFD10-03-P01
G1,G2,G3	Edmund	16-043	3	5mm Aperture, Protected Silver, Saturn 5B Single Axis Galvanometer Scanner https://www.edmundoptics.com/p/5mm-aperture-protected-silver-saturn-5b-single-axis-galvanometer-scanner/44530/
L1,L2,L3,L4,L5	Thorlabs	LSM54-1310	5	Scan Lens, 1200 to 1400 nm, EFL=54 mm https://www.thorlabs.com/thorproduct.cfm?partnumber=LSM54-1310
L6	Thorlabs	TL200-3P	1	Laser Scanning Tube Lens, f = 200 mm, ARC: 900 - 1900 nm https://www.thorlabs.com/thorproduct.cfm?partnumber=TL200-3P
OBJ	Thorlabs	N16XLWD-PF	1	16X Nikon CFI LWD Plan Fluorite Objective, 0.80 NA, 3.0 mm WD https://www.thorlabs.com/thorproduct.cfm?partnumber=N16XLWD-PF
DBS	Semrock	FF665-Di02-25x36	1	665 nm edge BrightLine® multiphoton single-edge dichroic beamsplitter https://www.idex-hs.com/store/product-detail/ff665_di02_25x36/fl-007042
L7	Thorlabs	LA1031-A	1	N-BK7 Plano-Convex Lens, Ø30.0 mm, f = 100 mm, AR Coating: 350 - 700 nm https://www.thorlabs.com/thorproduct.cfm?partnumber=LA1031-A
L8	Thorlabs	LA1131-A	1	N-BK7 Plano-Convex Lens, Ø1", f = 50 mm, AR Coating: 350 - 700 nm https://www.thorlabs.com/thorproduct.cfm?partnumber=LA1131-A
L9	Thorlabs	AC254-030-A	1	f = 30 mm, Ø1" Achromatic Doublet, ARC: 400 - 700 nm https://www.thorlabs.com/thorproduct.cfm?partnumber=AC254-030-A
F	Edmund	87-749	1	Bandpass filter, 520nm CWL, 25mm Dia, 70nm Bandwidth, OD 6 Fluorescence Filter https://www.meetoptics.com/filters/dielectric/bandpass-filter/s/edmund-optics/p/87-749?srsltid=AfmBOoq6GoGUlNTL2q1W0N_A4fyzoYjOs2AzgiiveZD6B2dGgYDwM5Kl
HPD	Hamamatsu	R11322U-40	1	Hybrid photo detector https://www.hamamatsu.com/us/en/product/optical-sensors/pmt/hpd/R11322U-40.html
TA	Femto	HCA-400M-5K-C	1	High Speed Transimpedance Amplifiers (Current Amplifiers) HCA https://www.femto.de/en/current-transimpedance-amplifiers/dc-up-to-400-mhz-fast-fixed-amplification-hca/
DAQ	Thorlabs	ThorDAQ	1	Data acquisition system
		Stage optomechanics		
	Thorlabs	PLSXY	1	2D Motorized Translation Stage for Rigid Stands https://www.thorlabs.com/thorproduct.cfm?partnumber=PLSXY
	Thorlabs	PT1-Z9	1	25 mm (0.98") One-Axis Motorized Translation Stage, 1/4"-20 Taps https://www.thorlabs.com/thorproduct.cfm?partnumber=PT1-Z9

List of components used to build LIFT. Abbreviations match those of the detailed setup figure (Supplementary Fig. 6)

Supplementary Table 3: Acquisition parameters for all figures

Figure	Animal	Dwell time (µs)	Avg. focal spot spacing (µm)	Frame rate (Hz)	Frames averaged	FOV geometry	Imaging type
3	Mouse	4	1	0.06	1-10	1	Structural
4, 5, S7, S8	Mouse	1	4	6	1	2	Activity
6	Rat	4	1	0.06	3-10	1	Structural
S11	Mouse	1	4	27	1	3	Activity
S12	Mouse	1	2	11	1	4	Activity

Figure	3a	3b	3c	3d	4c	4f	4i
Power on brain	10 - 141	55	81	141	91	101	125
Depth	0 - 1230	640	880	1065	930	981	1026
PO power	13 - 171	70	100	171	112	124	152

Figure	4l	5b	5f	6a	6b	6c	6d
Power on brain	141	101	64	21	36	55	65
Depth	1081	981	998	310	510	730	900
PO power	171	124	78	28	46	69	80

Figure	6e	6f	S5,S6	S9	S10
Power on brain	103	104	101	127	83
Depth	1100	1200	981	1005	900
PO Power	124	124	124	155	102

Acquisition parameters and excitation powers for all main text and supplementary figures. Due to the power absorbed in the immersion water, both post-objective (PO) powers and the powers on the brain surface are listed. S denotes supplementary figures, and the FOV geometries refer to the schematics shown in Supplementary Fig. 14.

References

[1] Demas, J., Manley, J., Tejera, F., Barber, K., Kim, H., Traub, F.M., Chen, B., Vaziri, A.: High-speed, cortex-wide volumetric recording of neuroactivity at cellular resolution using light beads microscopy. Nature Methods **18**(9), 1103–1111 (2021)

[2] Pnevmatikakis, E.A., Soudry, D., Gao, Y., Machado, T.A., Merel, J., Pfau, D., Reardon, T., Mu, Y., Lacefield, C., Yang, W., *et al.*: Simultaneous denoising, deconvolution, and demixing of calcium imaging data. Neuron **89**(2), 285–299 (2016)

[3] Mok, A.T., Wang, T., Zhao, S., Kolkman, K.E., Wu, D., Ouzounov, D.G., Seo, C., Wu, C., Fetcho, J.R., Xu, C.: A large field-of-view, single-cell-resolution two-and three-photon microscope for deep and wide imaging. eLight **4**(1), 20 (2024)

[4] Wang, T., Wu, C., Ouzounov, D.G., Gu, W., Xia, F., Kim, M., Yang, X., Warden, M.R., Xu, C.: Quantitative analysis of 1300-nm three-photon calcium imaging in the mouse brain. Elife **9**, 53205 (2020)

[5] Podgorski, K., Ranganathan, G.: Brain heating induced by near-infrared lasers during multiphoton microscopy. Journal of neurophysiology **116**(3), 1012–1023 (2016)

[6] Demmerle, J., Innocent, C., North, A.J., Ball, G., Müller, M., Miron, E., Matsuda, A., Dobbie, I.M., Markaki, Y., Schermelleh, L.: Strategic and practical guidelines for successful structured illumination microscopy. Nature protocols **12**(5), 988–1010 (2017)

[7] Oron, D., Papagiakoumou, E., Anselmi, F., Emiliani, V.: Two-photon optogenetics. Progress in brain research **196**, 119–143 (2012)

[8] Kong, L., Cui, M.: A high throughput ($> 90\%$), large compensation range, single-prism femtosecond pulse compressor. arXiv preprint arXiv:1306.5011 (2013)